

# The record low thermal conductivity of monolayer Cuprous Iodide (CuI) with direct wide bandgap

Jinyuan Xu<sup>1</sup>, Ailing Chen<sup>1</sup>, Linfeng Yu<sup>1</sup>, Huimin Wang<sup>2</sup>, and Guangzhao Qin<sup>1,\*</sup>

<sup>1</sup>*State Key Laboratory of Advanced Design and Manufacturing for Vehicle Body, College of Mechanical and Vehicle Engineering, Hunan University, Changsha 410082, P. R. China*

<sup>2</sup>*Hunan Key Laboratory for Micro-Nano Energy Materials & Device and School of Physics and Optoelectronics, Xiangtan University, Xiangtan 411105, Hunan, China*

**Abstract:** Two-dimensional materials have attracted lots of research interests due to the fantastic properties. In the microelectronics revolution, the semiconductors with wide bandgap take key position, where the bulk Cuprous Iodide in the cubic wurtzite phase ( $\gamma$ -CuI) is a *p*-type semiconductor with small effective mass. In this paper, from the *state-of-art* first-principles calculations, we predicted the stable structure of monolayer counterpart of the  $\gamma$ -CuI, and presented the multifunctional superiority by performing systematical study on the electronic, optical, and thermal transport properties. A direct bandgap is found in monolayer CuI (3.57 eV), which is larger than the  $\gamma$ -CuI (3.1 eV), leading to the better optical performance. Moreover, ultralow thermal conductivity is predicted for monolayer CuI (0.08 W/mK), which is much lower than the common semiconductors and close to that of air. The direct wide bandgap and the ultralow thermal conductivity of monolayer CuI would promise its potential applications in transparent and wearable electronics.

**Keywords:** first-principles, CuI, bandgap, visible transparency, thermal conductivity

## 1. Introduction

Since the discovery of graphene<sup>1</sup>, two-dimensional (2D) materials have attracted lots of research interests due to the fantastic properties. In particular, materials in the 2D form usually possess better performance than the bulk counterparts, and the properties regulation in 2D materials can be more effective due to the larger surface volume ratio. After years studies, numerous 2D materials have been reported and investigated, such as silicene<sup>2,3</sup>, phosphorene<sup>4</sup>, MoS<sub>2</sub><sup>5</sup>, *etc.* With the outstanding properties, the 2D materials have shown the potential applications in lots of fields, such as electronics<sup>6</sup>, optoelectronics,<sup>7</sup> thermoelectrics<sup>8</sup>, catalysis<sup>9</sup>, *etc.*

In the microelectronics revolution, the semiconductors with wide bandgap take key position. For instance, the Gallium Nitride (GaN) has been widely used for high-power electronics<sup>10</sup> and the blue light LEDs<sup>11</sup>, which was awarded the 2014 Nobel in Physics<sup>12</sup>. In addition, the Zinc Oxide (ZnO)<sup>13</sup> is also a widely used *n*-type semiconductor in the field of transparent electronics due to the direct bandgap of 3.4 eV. Among the candidates for the potential applications in transparent electronics, the *n*-type semiconductors usually have small effective mass while *p*-type semiconductors usually have large effective mass. However, it is found that the bulk  $\gamma$ -CuI in cubic wurtzite is a *p*-type semiconductor with small effective mass, which promise the high carrier mobility<sup>14</sup> benefiting applications coupled with *n*-type semiconductors. Moreover, the  $\gamma$ -CuI is found to possess potential applications in thermoelectrics<sup>15</sup> due to the large Seebeck coefficient.

Considering the successful cases in the past of the extraordinary properties of 2D materials as compared to the bulk counterparts, it is expected that the monolayer CuI could have better properties than the  $\gamma$ -CuI. In fact, the ultrathin 2D nanosheets of  $\gamma$ -CuI has already been synthesized<sup>16</sup>. However, it is in the form of film of the non-layered  $\gamma$ -CuI and the structure of the single-layer CuI would be different from the unit-layer in the  $\gamma$ -CuI film. Thus, it is necessary to uncover the structure of monolayer CuI for future studies. In addition, the electronic and optical properties of monolayer CuI are of great significance to the potential

applications in transparent electronics, which are unclear. Moreover, the thermal transport properties demand for fundamental study for its applications in more valuable fields such as wearable electronics.

In this paper, from the *state-of-art* first-principles calculations, we predicted the stable structure of monolayer CuI and presented the multifunctional superiority by performing systematical study on the electronic, optical, and thermal properties. A direct bandgap is found in monolayer CuI, which is larger than the  $\gamma$ -CuI, leading to the better optical performance. Moreover, ultralow thermal conductivity is predicted for monolayer CuI, which is much lower than the commonly used semiconductors. The direct wide bandgap and the ultralow thermal conductivity of monolayer CuI would promise its potential applications in transparent and wearable electronics.

## 2. Results and discussion

### 2.1 The structure and the stability of monolayer CuI

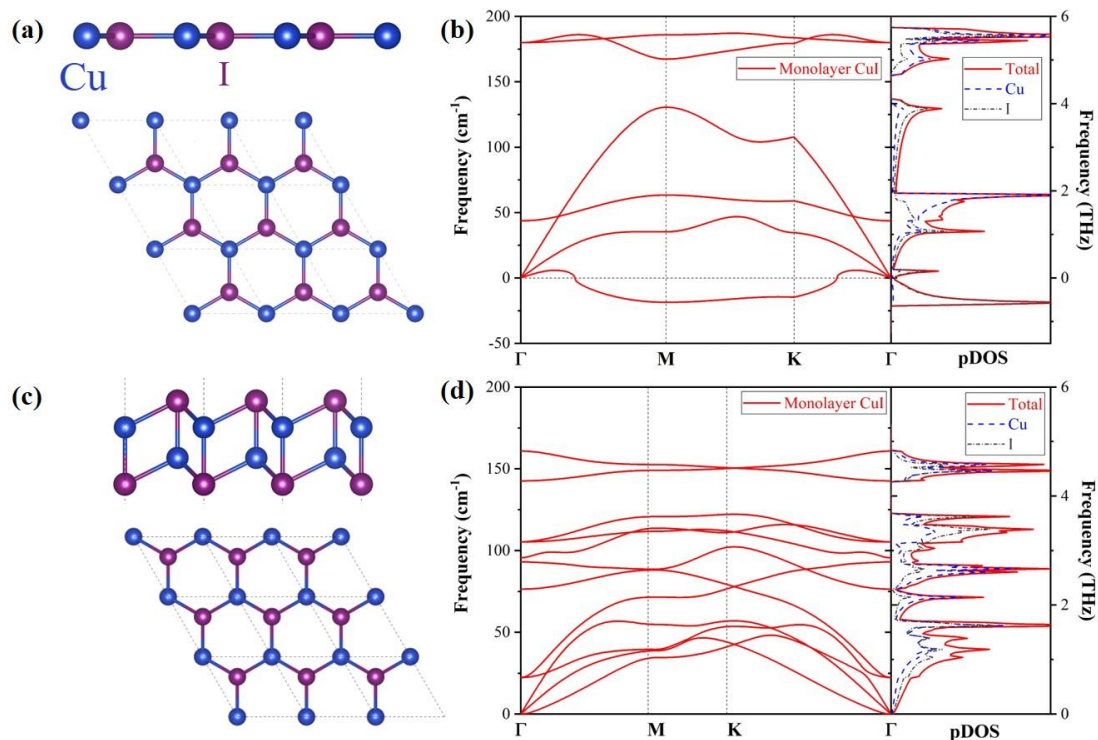


Figure 1. The stable structure of monolayer CuI verified by the phonon dispersions. (a) The planar structure of monolayer CuI similar to graphene and (b) the corresponding phonon

dispersion with negative frequencies. (c) The buckled structure of monolayer CuI and (d) the corresponding phonon dispersion with no negative frequency. The partial density of states (pDOS) are also presented.

As reported in previous studies, 2D materials are commonly formed in a few typical structures<sup>17</sup>, such as the hexagonal honeycomb structure represented by graphene, the hinge-like puckered structure represented by phosphorene, the sandwich structure represented by MoS<sub>2</sub>, the buckled structure represented by silicene, *etc.* Thus, for exploring the stable structure of monolayer CuI, it would be of high efficiency to construct the monolayer CuI in the pattern of the common structures in 2D, and further verify the structural stability based on the lattice dynamics by calculating the phonon dispersions.

By testing all the possible patterns of structures for 2D materials, it is found that negative frequency exists for monolayer CuI except the buckled structure as shown in Fig. 1(c,d). The monolayer CuI in the planar hexagonal honeycomb structure similar to graphene is presented here as a contrast, and the negative frequencies in the phonon dispersion reveals the unstable nature [Fig. 1(a,b)]. Thus, by examining the stability of monolayer CuI in different patterns of 2D structures, the stable structure of monolayer CuI is successfully found with two buckled sublayers, showing similar characteristics as silicene.

There are four atoms in the primitive cell of monolayer CuI and the vibration frequency is low, which may lie in the heavy atomic masses. By examining the pDOS of the lattice vibration, it is found that the Cu and I atoms contribute near equally at different frequencies. Moreover, there exists a bandgap among the optical phonon branches, which may lead to the weakened scattering of optical phonon modes as reported previously.

## **2.2 The direct wide bandgap and visible transparency**

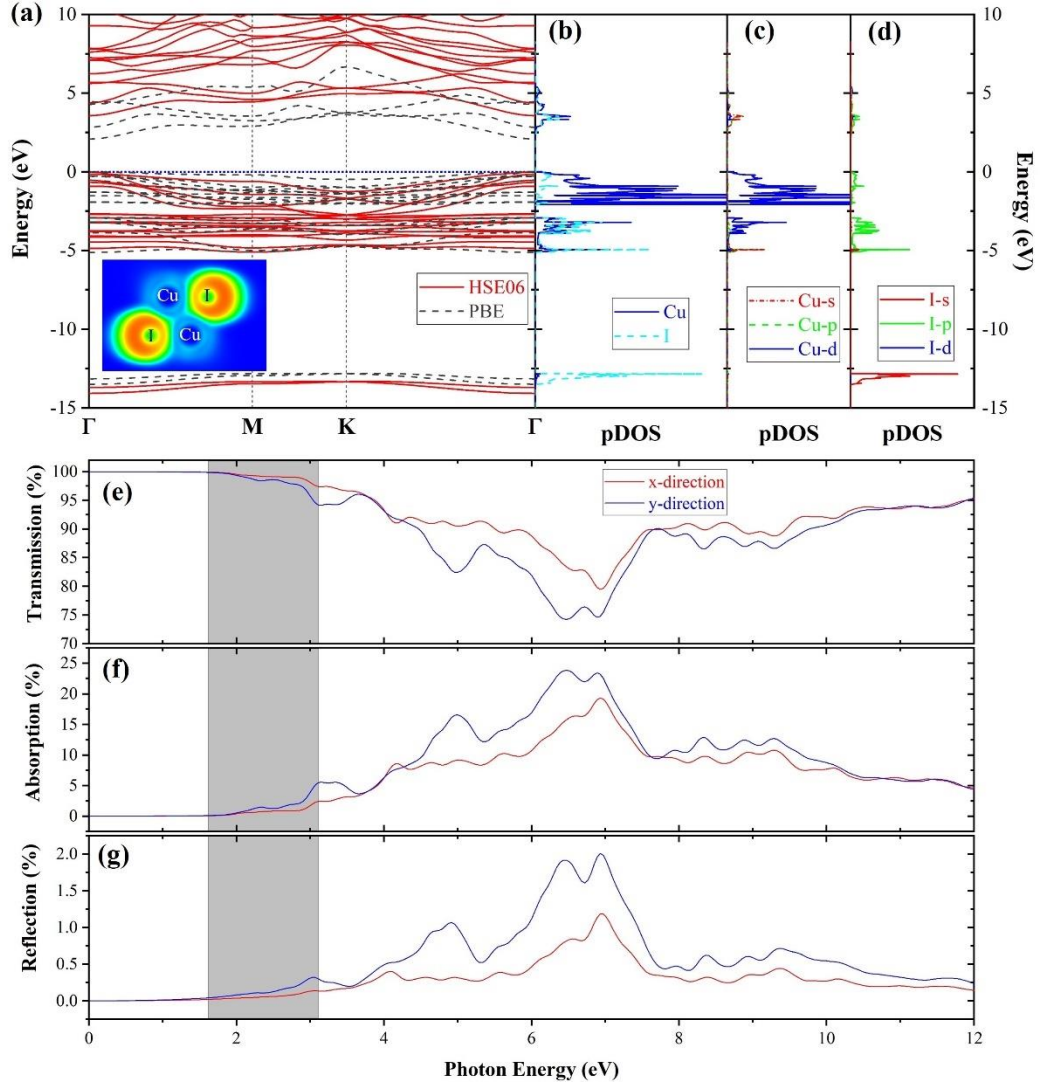


Figure 2. The electronic structures and the optical properties of monolayer CuI. (a) The electronic band structures calculated by PBE and HSE06, and (b-d) the orbital projected density of states (pDOS). The (e) transmission, (f) absorption, and (g) reflection coefficient.

With the verified stable structure of monolayer CuI, the electronic structures are investigated as shown in Fig. 2(a). Using the PBE functional, a direct bandgap is predicted in monolayer CuI and the conduction band minimum (CBM) and valence band maximum (VBM) locate at the Gamma point. The bandgap is predicted as 2.07 eV by PBE, which is widely recognized to be underestimated. To accurately predict the bandgap of monolayer CuI, we utilize the HSE06 and obtain the bandgap being 3.57 eV. The bandgap keeps to be direct with HSE06

used, which promises the potential applications of monolayer CuI in electronics and optoelectronics since phonon is not required for electron transition. Moreover, the bandgap of monolayer CuI (3.57 eV) is larger than that of bulk  $\gamma$ -CuI (3.1 eV)<sup>15</sup>, making monolayer CuI a better direct wide bandgap semiconductor. In addition, the VBM is found to be mainly contributed by the Cu-*d* orbital as indicated by the pDOS in Fig. 2 (b-d).

Furthermore, the linear optical properties of monolayer CuI are investigated based on the precise electronic structures obtained from HSE06, and the absorption coefficient  $\alpha(\omega)$ , refractive coefficient  $R(\omega)$  and reflection coefficient  $n(\omega)$  of CuI can be obtained [Fig. 2 (b-d)] as<sup>18–20</sup>:

$$\alpha(\omega) = \frac{2\omega k(\omega)}{c} = \frac{\varepsilon_2(\omega)\omega}{n(\omega)c}$$

$$R(\omega) = \frac{[n(\omega) - 1]^2 + k(\omega)^2}{[n(\omega) + 1]^2 + k(\omega)^2}$$

$$n(\omega) = \frac{1}{\sqrt{2}} \left[ \sqrt{\varepsilon_1(\omega)^2 + \varepsilon_2(\omega)^2} + \varepsilon_1(\omega) \right]^{\frac{1}{2}}$$

where  $\varepsilon_1(\omega)$  and  $\varepsilon_2(\omega)$  are the real and imaginary parts of the dielectric function, respectively. The term  $k(\omega)$  is the extinction coefficient, which can be derived by:<sup>18,19</sup>

$$k(\omega) = \frac{1}{\sqrt{2}} \left[ \sqrt{\varepsilon_1(\omega)^2 + \varepsilon_2(\omega)^2} - \varepsilon_1(\omega) \right]^{\frac{1}{2}}$$

The real  $\varepsilon_1(\omega)$  can be obtained by the Kramers–Kronig relation<sup>18</sup>:

$$\varepsilon_1(\omega) = 1 + \frac{2}{\pi} P \int_0^{\infty} \frac{\varepsilon_2(\alpha)\alpha d\alpha}{\alpha^2 - \omega^2}$$

and imaginary parts  $\varepsilon_2(\omega)$  can be derived by<sup>21</sup> :

$$\varepsilon_2(\omega) = \frac{4\pi^2 e^2}{m^2 \pi^2} \times \sum_{C,V} |M_{C,V}|^2 \delta(E_C + E_V - \hbar\omega)$$

The terms  $e$ ,  $m$ , and  $\omega$  are electron charge, effective mass, and angular frequency, respectively.

The terms  $C$  and  $V$  represent the conduction band and valence band, respectively. The term  $M$

represents the momentum transfer matrix. The term  $E$  is the electron energy level, and the delta function  $\delta$  can enhance the energy conversion of electrons during the transition from band to band.

As shown in Fig. 2(e-g), in the energy domain of 0 - 7 eV, the absorption [Fig. 2(f)] and refraction [Fig. 2 (g)] coefficients of monolayer CuI increase continuously, which means that monolayer CuI has an enhanced ability to absorb and refract light in this region. Correspondingly, the photon transmission [Fig. 2 (e)] capability of monolayer CuI becomes weaker as the transmission coefficient decreases. When the photon energy is larger than 7 eV, the absorption and refraction coefficients of CuI begin to weaken significantly, and finally reach a plateau at the energy threshold of 8 eV. It is worth noting that compared with the absorption and transmission capabilities of phonons, the reflection efficiency of monolayer CuI for photons is low, up to no more than 2%. For photon absorption, the working region of monolayer CuI is in the energy region of 5.0 - 7.5eV, while the photon energy of visible light is between 1.62 and 3.11 eV. Obviously, the main absorption light of CuI is ultraviolet light, up to 20%.

### 2.3 The ultralow thermal conductivity

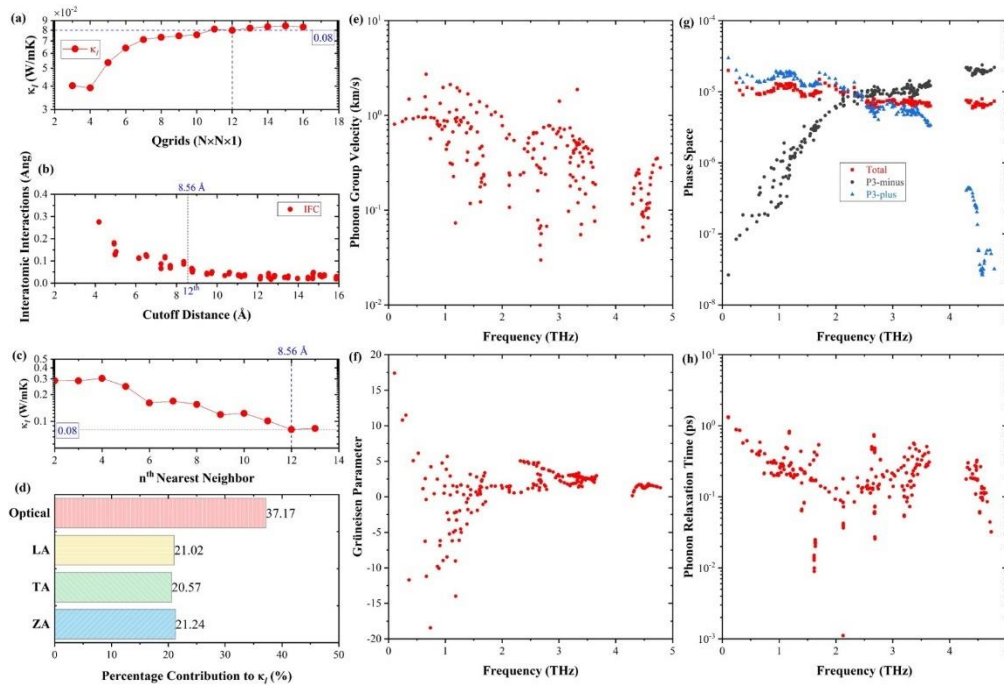


Figure. 3. The thermal transport properties of monolayer CuI at 300 K. (a) The convergence of thermal conductivity with respect to the  $Q$ -grid. (b) The variation of interatomic interactions with respect to the atomic distance. (c) The convergence of thermal conductivity with respect to the cutoff distance. (d) The contribution from different branches of out-of-plane  $z$ -direction (ZA), traverse (TA), and longitudinal (LA) acoustic and optical phonon. (e-h) The modal analysis for (e) group velocity, (f) Grüneisen parameter, (g) phase space, and (h) phonon relaxation time.

The thermal transport properties of monolayer CuI are also investigated, which is crucial for its practical applications in devices. The thermal conductivity is calculated by solving the phonon Boltzmann transport equation (BTE) based on first-principles calculations with no adjustable parameters. With full convergence test, the thermal conductivity of monolayer CuI is predicted as 0.08 W/mK [Fig. 3(c)] at 300 K, which is a record low value close to the thermal conductivity of air. The ultralow thermal conductivity of monolayer CuI is much lower than the most of already known semiconductor. The underlying reason may lie in the heavy atoms of Cu and I, and also the buckled structure of monolayer CuI. Consequently, the group velocity is low and the scattering phase space is large. In addition, the phonon anharmonicity is found strong in monolayer CuI. Thus, the ultralow thermal conductivity emerges in monolayer CuI, which would benefit the applications of power supply in wearable devices or IoT by promising excellent thermoelectric performance.

When performing the convergence test, it is found that the thermal conductivity decreases with the increasing cutoff distance, and a few stages are presented. The decreasing thermal conductivity is due to the inclusion of more interatomic interactions and more phonon-phonon scattering. Note that the thermal conductivity still presents a decrease at large cutoff distance ( $>6 \text{ \AA}$ ), which reveals the long-range interactions in monolayer CuI. Such long-range interactions usually exist in materials with resonant bondings, such as phosphorene<sup>22</sup> and PbTe<sup>23</sup>. Finally, the convergence of thermal conductivity is verified by the analysis of



interatomic interactions<sup>24</sup> [Fig. 3(b)]. Moreover, detailed analysis reveals that the large contribution of optical phonon modes [Fig. 3(d)] is due to the relatively small phase space at the corresponding frequencies, which is resulted from the bandgap among the optical phonon branches as revealed in Fig. 1(d).

### 3. Conclusion

In summary, from the *state-of-art* first-principles, by examining the stability of monolayer CuI in different patterns of 2D structures, we predicted the stable structure of monolayer CuI as the counterpart of bulk  $\gamma$ -CuI, which possesses two buckled sublayers, showing similar characteristics as silicene. We presented the multifunctional superiority of monolayer CuI by performing systematical study on the electronic, optical, and thermal transport properties. A direct bandgap is found in monolayer CuI (3.57 eV), which is larger than the bulk  $\gamma$ -CuI (3.1 eV), leading to the better optical performance. Moreover, ultralow thermal conductivity is predicted for monolayer CuI (0.08 W/mK), which is much lower than the common semiconductors and close to that of air. The direct wide bandgap and the ultralow thermal conductivity of monolayer CuI would promise its potential applications in transparent and wearable electronics.

### 4. Computational methodology

All the first-principles calculations are implemented by the Vienna *ab initio* simulation package (VASP)<sup>25</sup> within the framework of density functional theory (DFT). The interaction between valence electrons and ion cores is performed by Projector augmented wave (PAW)<sup>26</sup> method. The Perdew-Burke-Ernzerhof (PBE) functional was chosen as the exchange-correlation functional for geometric structure optimization and thermal transport properties. Furthermore, the hybridized HSE06 functional was used to obtain precise electrical and optical properties. To prevent the periodic mirroring interaction along out-of-plane direction, 16 Å is used as a vacuum

layer. 920 eV is selected as the kinetic energy cutoff to expand the wave functions for plane wave basis with a Gamma centered grid<sup>27</sup> k-meshes of 8×8×1 to sample the irreducible Brillouin zone (IBZ). For geometric optimization, the energy convergence threshold of 10<sup>-8</sup> eV implemented until the Hellmann-Feynman force convergence accuracy of -5×10<sup>-7</sup> eV/Å. A 6×6×1 supercell is used for 2<sup>nd</sup> and 3<sup>rd</sup> force constants calculations.

The thermal conductivity is obtained as implemented in the ShengBTE package<sup>28,29</sup> by summing all the phonon mode ( $\lambda$ ) contributions:

$$\kappa = \kappa_{\alpha\alpha} = \frac{1}{V} \sum_{\lambda} C_{\lambda} v_{\lambda\alpha}^2 \tau_{\lambda\alpha}, \quad (1)$$

where  $V$  is the lattice volume associated with the effective thickness, and 7.8148 Å is chosen as the effective thickness. In addition,  $C_{\lambda}$ ,  $v_{\lambda\alpha}$ , and  $\tau_{\lambda\alpha}$  are the specific heat capacity, group velocity and relaxation time. Moreover, they can be further obtained through lattice dynamics. The phonon scattering rate is inversely proportional to the relaxation time, *i.e.*,  $\Gamma = \frac{1}{\tau}$ . The scattering rate is obtained by summing the different scattering terms based on Matthiessen's rule<sup>30</sup>:

$$\frac{1}{\tau(\vec{q}, p)} = \frac{1}{\tau^{anh}(\vec{q}, p)} + \frac{1}{\tau^{iso}(\vec{q}, p)} + \frac{1}{\tau^B(\vec{q}, p)}, \quad (2)$$

where  $1/\tau^{anh}$ ,  $1/\tau^{iso}$ , and  $1/\tau^B$  is the intrinsic three-phonon scattering rate, the scattering rate due to isotope impurities, and boundary scattering rate due to the finite length of sample. More importantly, the three-phonon scattering rate  $\Gamma_{\lambda\lambda'\lambda''}^{\pm}$  can be further obtained by<sup>5,7-9</sup>:

$$\Gamma_{\lambda\lambda'\lambda''}^+ = \frac{\hbar\pi}{4} \frac{f_0' - f_0''}{\omega_{\lambda}\omega_{\lambda'}\omega_{\lambda''}} |V_{\lambda\lambda'\lambda''}^+|^2 \delta(\omega_{\lambda''} + \omega_{\lambda'} - \omega_{\lambda}), \quad (7)$$

$$\Gamma_{\lambda\lambda'\lambda''}^- = \frac{\hbar\pi f_0' + f_0'' + 1}{4 \omega_\lambda \omega_{\lambda'} \omega_{\lambda''}} |V_{\lambda\lambda'\lambda''}^-|^2 \delta(\omega_{\lambda''} - \omega_{\lambda'} - \omega_\lambda), \quad (8)$$

where the scattering rate  $\Gamma_{\lambda\lambda'\lambda''}^+$  and  $\Gamma_{\lambda\lambda'\lambda''}^-$  are determined by the absorption emission process, respectively. In addition,  $\hbar$ ,  $\omega$ ,  $V_{\lambda\lambda'\lambda''}^\pm$ ,  $\delta$ , and  $f_0$  are Planck's constant, phonon frequency, the scattering matrix elements, the Dirac delta distribution function and the Bose-Einstein function, respectively.

## Acknowledgments

This work is supported by the National Natural Science Foundation of China (Grant No. 52006057), the Fundamental Research Funds for the Central Universities (Grant Nos. 531119200237, and 541109010001), the Changsha Municipal Natural Science Foundation (Grant No. kq2014034), and the State Key Laboratory of Advanced Design and Manufacturing for Vehicle Body at Hunan University (Grant No. 52175011). The numerical calculations in this paper have been done on the supercomputing system of the National Supercomputing Center in Changsha and Zhengzhou.

**Note:** During the preparation of the manuscript, we noticed that the monolayer CuI was synthesized very recently, which has the same structure as predicted in this work.

## References

1. Novoselov, K. S. *et al.* Electric Field Effect in Atomically Thin Carbon Films. *Science* **306**, 666–669 (2004).
2. Vogt, P. *et al.* Silicene: Compelling Experimental Evidence for Graphenelike Two-Dimensional Silicon. *Phys. Rev. Lett.* **108**, 155501 (2012).
3. Kara, A. *et al.* A review on silicene — New candidate for electronics. *Surf. Sci. Rep.* **67**, 1–18 (2012).
4. Carvalho, A. *et al.* Phosphorene: from theory to applications. *Nat. Rev. Mater.* **1**, 1–16 (2016).

5. Li, Y. *et al.* MoS<sub>2</sub> Nanoparticles Grown on Graphene: An Advanced Catalyst for the Hydrogen Evolution Reaction. *J. Am. Chem. Soc.* **133**, 7296–7299 (2011).
6. Kang, S. *et al.* 2D semiconducting materials for electronic and optoelectronic applications: potential and challenge. *2D Mater.* **7**, 022003 (2020).
7. Cheng, J., Wang, C., Zou, X. & Liao, L. Recent Advances in Optoelectronic Devices Based on 2D Materials and Their Heterostructures. *Adv. Opt. Mater.* **7**, 1800441 (2019).
8. Li, D. *et al.* Recent Progress of Two-Dimensional Thermoelectric Materials. *Nano-Micro Lett.* **12**, 36 (2020).
9. Deng, D. *et al.* Catalysis with two-dimensional materials and their heterostructures. *Nat. Nanotechnol.* **11**, 218–230 (2016).
10. Roccaforte, F., Fiorenza, P., Lo Nigro, R., Giannazzo, F. & Greco, G. Physics and technology of gallium nitride materials for power electronics. *Riv. Nuovo Cimento* **41**, 625–681 (2018).
11. Morkoç, H. & Mohammad, S. N. High-Luminosity Blue and Blue-Green Gallium Nitride Light-Emitting Diodes. *Science* (1995) doi:10.1126/science.267.5194.51.
12. Von Dollen, P., Pimputkar, S. & Speck, J. S. Let There Be Light—With Gallium Nitride: The 2014 Nobel Prize in Physics. *Angew. Chem. Int. Ed.* **53**, 13978–13980 (2014).
13. Hussain, B., Akhtar Raja, M. Y., Lu, N. & Ferguson, I. Applications and synthesis of zinc oxide: An emerging wide bandgap material. in *2013 High Capacity Optical Networks and Emerging/Enabling Technologies* 88–93 (2013). doi:10.1109/HONET.2013.6729763.
14. Yamada, N., Ino, R. & Ninomiya, Y. Truly Transparent p-Type  $\gamma$ -CuI Thin Films with High Hole Mobility. *Chem. Mater.* **28**, 4971–4981 (2016).
15. Yang, C. *et al.* Transparent flexible thermoelectric material based on non-toxic earth-abundant p-type copper iodide thin film. *Nat. Commun.* **8**, 16076 (2017).
16. Yao, K. *et al.* Synthesis of ultrathin two-dimensional nanosheets and van der Waals heterostructures from non-layered  $\gamma$ -CuI. *Npj 2D Mater. Appl.* **2**, 1–7 (2018).

17. Mannix, A. J., Kiraly, B., Hersam, M. C. & Guisinger, N. P. Synthesis and chemistry of elemental 2D materials. *Nat. Rev. Chem.* **1**, 1–14 (2017).
18. Houmad, M., Zaari, H., Benyoussef, A., El Kenz, A. & Ez-Zahraouy, H. Optical conductivity enhancement and band gap opening with silicon doped graphene. *Carbon* **94**, 1021–1027 (2015).
19. Wang, J., Li, Z., Jia, Y., Wang, B. & Xu, Z. Molecular dynamics simulation of effect of temperature on Cu nanoparticles agglomeration of nanofluids. *J. Nanoparticle Res.* **23**, 28 (2021).
20. Schlüter, M. *et al.* Optical properties of GaSe and Ga S x Se 1 – x mixed crystals. *Phys. Rev. B* **13**, 3534–3547 (1976).
21. Wang, H. *et al.* First-principles study of electronic, optical and thermal transport properties of group III–VI monolayer MX (M = Ga, In; X = S, Se). *J. Appl. Phys.* **125**, 245104 (2019).
22. Qin, G. *et al.* Resonant bonding driven giant phonon anharmonicity and low thermal conductivity of phosphorene. *Phys. Rev. B* **94**, 165445 (2016).
23. Li, C. W. *et al.* Anharmonicity and atomic distribution of SnTe and PbTe thermoelectrics. *Phys. Rev. B* **90**, 214303 (2014).
24. Qin, G. & Hu, M. Accelerating evaluation of converged lattice thermal conductivity. *Npj Comput. Mater.* **4**, 1–6 (2018).
25. Kresse, G. & Hafner, J. *Ab initio* molecular-dynamics simulation of the liquid-metal–amorphous-semiconductor transition in germanium. *Phys. Rev. B* **49**, 14251–14269 (1994).
26. Kresse, G. & Joubert, D. From ultrasoft pseudopotentials to the projector augmented-wave method. *Phys. Rev. B* **59**, 1758–1775 (1999).
27. Monkhorst, H. J. & Pack, J. D. Special points for Brillouin-zone integrations. *Phys. Rev. B* **13**, 5188–5192 (1976).

28. Li, W., Lindsay, L., Broido, D. A., Stewart, D. A. & Mingo, N. Thermal conductivity of bulk and nanowire  $\text{Mg}_{2-x}\text{Si}_x\text{Sn}_{1-x}$  alloys from first principles. *Phys. Rev. B* **86**, 174307 (2012).
29. Li, W., Carrete, J., A. Katcho, N. & Mingo, N. ShengBTE: A solver of the Boltzmann transport equation for phonons. *Comput. Phys. Commun.* **185**, 1747–1758 (2014).
30. Qin, Z., Qin, G., Zuo, X., Xiong, Z. & Hu, M. Orbitally driven low thermal conductivity of monolayer gallium nitride (GaN) with planar honeycomb structure: a comparative study. *Nanoscale* **9**, 4295–4309 (2017).